

Aneuploidy may be an evolutionary sidetrack on the path to adaptation

Ilia Kohanovski^{1,2,*}, Martin Pontz^{1,*}, Avihu H. Yona³, and Yoav Ram^{1,†}

¹School of Zoology, Faculty of Life Sciences, Tel Aviv University, Tel Aviv, Israel

²School of Computer Science, Reichman University, Herzliya, Israel

³Institute of Biochemistry, Food Science and Nutrition, Robert H. Smith Faculty of Agriculture, Food and Environment, The Hebrew University of Jerusalem, Israel

*These authors contributed equally to this work

†Corresponding author: yoav@yoavram.com

July 18, 2022

Abstract

BLA

Classifications. Biological Sciences: Evolution, Genetics, Microbiology, Population Biology.

Keywords: aneuploidy, evolutionary model, adaptive evolution

Introduction

Aneuploidy is an imbalance in the number of chromosomes in the cell: an incorrect karyotype. Evidence suggests aneuploidy is very common in eukaryotes, e.g. animals^{32,24,2}, and fungi^{27,53,30,44}. Aneuploidy has been implicated in cancer formation and progression^{3,34,32}. It is also common in protozoan pathogens of the *Leishmania* genus, a major global health concern²², and contributes to the emergence of drug resistance³⁵ and virulence²³ in fungal pathogens, which are under-studied³¹, despite infecting a billion people per year, causing significant morbidity in >150 million and death in >1.5 million people per year^{35,31}.

Experiments with human and mouse embryos found that aneuploidy is usually lethal. It is also associated with developmental defects and lethality in other multicellular organisms³⁸. For example, aneuploid mouse embryonic cells grow slower than euploid cells⁴⁹. Similarly, in unicellular eukaryotes growing in benign conditions, aneuploidy usually leads to slower growth and decreased overall fitness^{25,47,27,38,16,50}, in part due to proteotoxic stress caused by increased expression in aneuploid cells^{27,33,52} and hypo-osmotic-like stress⁴⁸.

However, aneuploidy can be beneficial under stressful conditions due to the wide range of phenotypes it can produce, some of which are advantageous^{27,50}. Thus, aneuploidy can lead to rapid adaptation in unicellular eukaryotes^{11,46,13,29}, as well as to rapid growth of somatic tumour cells^{34,40}. For example, aneuploidy in *Saccharomyces cerevisiae* facilitates adaptation to a variety of stressful conditions like heat and pH⁵¹, copper^{4,11}, salt⁷, and nutrient limitation^{8,12,1}, with similar results in *Candida albicans*⁵⁰. Importantly, aneuploidy can also lead to drug resistance in pathogenic fungi such as *C. albicans*^{37,36,10} and *Cryptococcus neoformans*⁴¹, which cause candidiasis and meningoencephalitis, respectively.

Experimental evidence for the role of aneuploidy in adaptive evolution was demonstrated by Yona et al.⁵¹. They evolved populations of *S. cerevisiae* under strong heat stress. The populations adapted to the heat stress within 450 generations, and this adaptation was determined to be due a duplication of chromosome III. Later on, after more than 1,500 generations, the populations reverted back to an euploid state, while remaining adapted to the heat stress. The authors hypothesized that aneuploidy is a *transient adaptive solution*, because it can rapidly appear and fixate in the population under stressful conditions, and can then be rapidly lost when the cost of aneuploidy outweighs its benefit—after the stress is removed, or after "refined" beneficial mutations appear and fixate.

Here, we test the hypothesis that aneuploidy is a *transient adaptive solution*. First, we analyze previously unpublished sequencing data from the original experimental populations of Yona et al.⁵¹

to assess if the aneuploid population and the evolved euploid population carry the same mutant alleles, as expected if the later is descended from the former. Second, we develop an evolutionary genetic model and fit it to the experimental results of Yona et al.⁵¹ in order to predict the genotype frequency dynamics in the experimental populations, thereby estimating the frequency of evolved euploid cells that descended from aneuploid cells. Our results show that, despite aneuploidy having reached high frequencies in the experimental populations, the majority of cells in the evolved euploid populations likely did not descend from aneuploid cells, but rather directly from wild-type euploid cells. These results suggest that aneuploidy may have been a sidetrack, rather than a stepping stone, on the path to adaptation.

Results

In the heat-stress experiment of Yona et al.⁵¹, four populations of *S. cerevisiae* evolved under 39 °C. Aneuploidy fixed in all four experimental repetitions in the first 450 generations. Two of the repetitions, marked *H2* and *H4*, carried no large-scale duplications other than a chromosome III trisomy. These two repetitions continued to evolve under the same conditions, wherein aneuploidy was eliminated by generation 1,700 and 2,350.

Empirical frequencies of mutant alleles. Our first test of the *transient adaptive solution hypothesis* employs previously unpublished sequencing data. For each of two evolved populations (*H2* and *H4*) we sequenced the ancestral population (generation zero), the aneuploid population (generation 450), and the evolved euploid population (generation 1,700 or 2,350) to estimate the mutant allele frequencies (??). Overall, between 100 and 173 mutant alleles were detected with at least a single read in the six population that were sampled. Disregarding 45 and 40 alleles that were present in the ancestral populations at a frequency >10%, the aneuploid and euploid populations carried a large number of mutant alleles: 82 and 95, respectively, in repetition *H2*, and 60 and 66 in repetition *H4*.

Surprisingly, out of all these mutant alleles, none was present at a frequency >20% in both the aneuploid and the evolved euploid populations. Furthermore, a high mutant allele frequency in the aneuploid population implies a low frequency in the evolved euploid population, and vice-versa (Spearman's correlation coefficient $\rho = -0.64$ and -0.66 in the two experimental repetitions; Figure 1), such that mutant alleles frequent in the aneuploid populations decreased in frequency when aneuploidy was lost. Moreover, for the 18 mutant alleles with high frequency in the aneuploid populations (>20%), the highest frequencies in the euploid populations were 15.4%, 16%, 16.3% and 19.6% (the rest were below

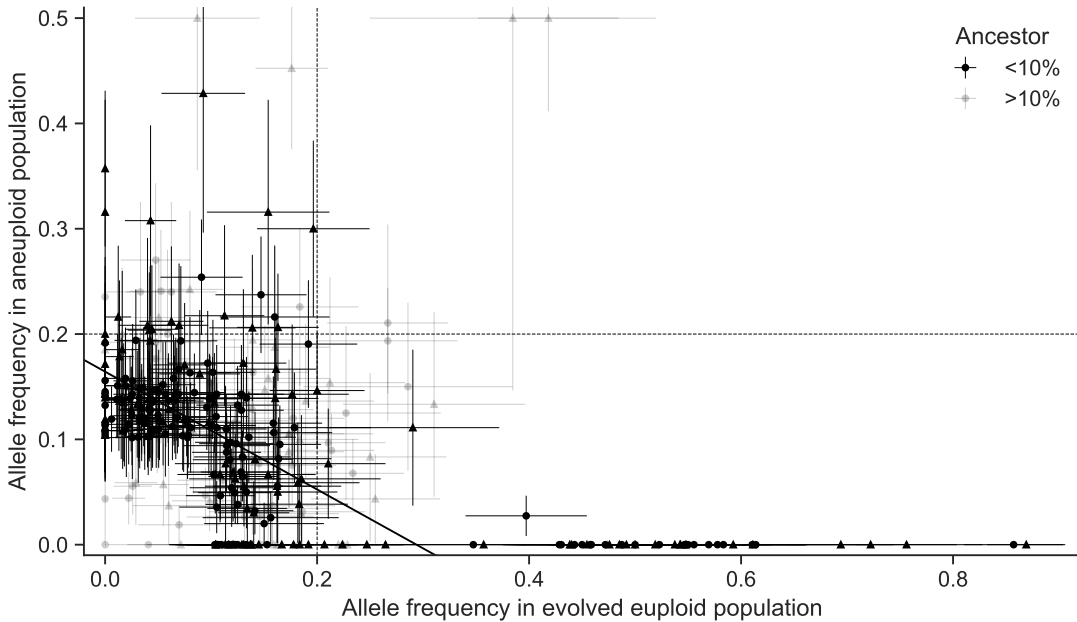


Figure 1: Frequencies of mutant alleles in the experimental populations are negatively correlated. Frequencies of mutant alleles when trisomy was widespread in the population (y-axis) and after it was eliminated (x-axis) in two experimental repetitions (circles for $H2$ and triangles for $H4$) from Yona et al.⁵¹. Mutant alleles with $>20\%$ in the aneuploid population were $<20\%$ in the euploid population, and vice versa (the upper-right quadrant is empty), suggesting that the majority of evolved euploid cells did not descend from the most common aneuploid genotypes. Alleles with frequency below and above 10% in the ancestral populations are in black and gray, respectively. Solid black line is a linear orthogonal distance regression line (slope= -0.559 , intercept=0.164). Dashed vertical and horizontal lines show allele frequencies 20%. Error bars show standard error of the mean accounting for the number of reads.

15%). Similarly, for the 48 mutant alleles with high frequency in the evolved euploid populations, the highest frequencies in the aneuploid populations were 2.7%, 7.7%, and 11.1% (the rest were below 1%). These results suggest evolved euploid cells are unlikely to descend from aneuploid cells.

Evolutionary genetic model. To further test the *transient adaptive solution hypothesis*, we developed an evolutionary genetic model, fitted the model to empirical data, and used it to predict the genotype frequency dynamics, or specifically, the fraction of the evolved euploid population descended from aneuploid cells.

The model includes the effects of natural selection, genetic drift, aneuploidy, and mutation, and follows a population of cells characterized by both their genotype: euploid wild-type, $2n$, is the ancestral diploid genotype; euploid mutant, $2n^*$, has a diploid karyotype and a single beneficial

mutation; aneuploid wild-type, $2n+1$, has an extra chromosome due to a chromosome duplication event; and aneuploid mutant, $2n+1^*$, has an extra chromosome and a beneficial mutation. Fitness values of the different genotypes are denoted by w_{2n} , w_{2n^*} , w_{2n+1} , and w_{2n+1^*} , and the rate of mutation and aneuploidy are denoted by μ and δ . See Figure 2 for an illustration of the model.

We fitted this model to the experimental results⁵¹ – time for fixation and for loss of aneuploidy – using approximate Bayesian computation with sequential Monte Carlo, or ABC-SMC⁴², thereby inferring the model parameters: rates and fitness effects of aneuploidy and mutation. We then sampled posterior predictions for the genotype frequency dynamics using the estimated parameter values and compared different versions of the model to test additional hypotheses about the evolutionary process.

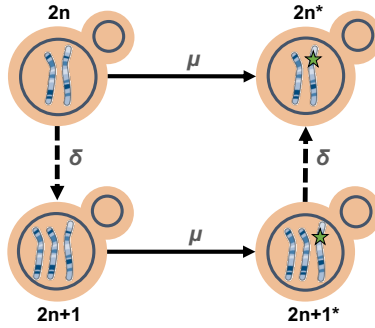


Figure 2: Model Illustration. There are four genotypes in our model: euploid wild-type, $2n$; euploid mutant, $2n^*$; aneuploid wild-type, $2n+1$; and aneuploid mutant, $2n+1^*$. Overall there are two possible trajectories from $2n$ to $2n^*$. Arrows denote transitions between genotypes, with transition rates μ for the beneficial mutation rate and δ for the aneuploidy rate.

Estimated rates and fitness effects of aneuploidy and mutation. We inferred the posterior distribution of model parameters (Figure 3). We report parameter estimates using the MAP (maximum a posteriori) and providing the 50% HDI (highest density interval) in square brackets. See *Supporting material* for sensitivity analysis. The estimated mutation rate, $\mu = 2.965 \cdot 10^{-6}$ [$2.718 \cdot 10^{-7} - 3.589 \cdot 10^{-6}$], corresponds to a mutation target size of $\sim 10^4$, assuming the mutation rate per base pair is roughly $2 \cdot 10^{-1054}$ or $3.3 \cdot 10^{-1021}$. The estimated aneuploidy rate, $\delta = 1.72 \cdot 10^{-3}$ [$1.47 \cdot 10^{-3} - 2.786 \cdot 10^{-3}$] is much higher than in previous studies: for chromosome III in diploid *S. cerevisiae*, Zhu et al.⁵⁴ estimated $6.7 \cdot 10^{-6}$ chromosome gain events per generation, and Kumaran et al.²⁰ estimate $3.0 - 4.3 \cdot 10^{-5}$ chromosome loss events per generation (95% confidence interval). The estimated fitness values are $w_{2n+1} = 1.022$ [$1.021 - 1.023$], $w_{2n+1^*} = 1.025$ [$1.024 - 1.026$], $w_{2n^*} = 1.028$ [$1.026 - 1.029$], all relative to the fitness of $2n$, which is set to $w_{2n} = 1$. Thus, we can infer that the cost of trisomy is $c = w_{2n^*} - w_{2n+1^*} = 0.003$ (or 0.3%) and the benefit of trisomy is $w_{2n+1} - 1 - c = 0.019$ (1.9%).

whereas the benefit of beneficial mutation is $w_{2n^*} - 1 = 0.028$ (2.8%).

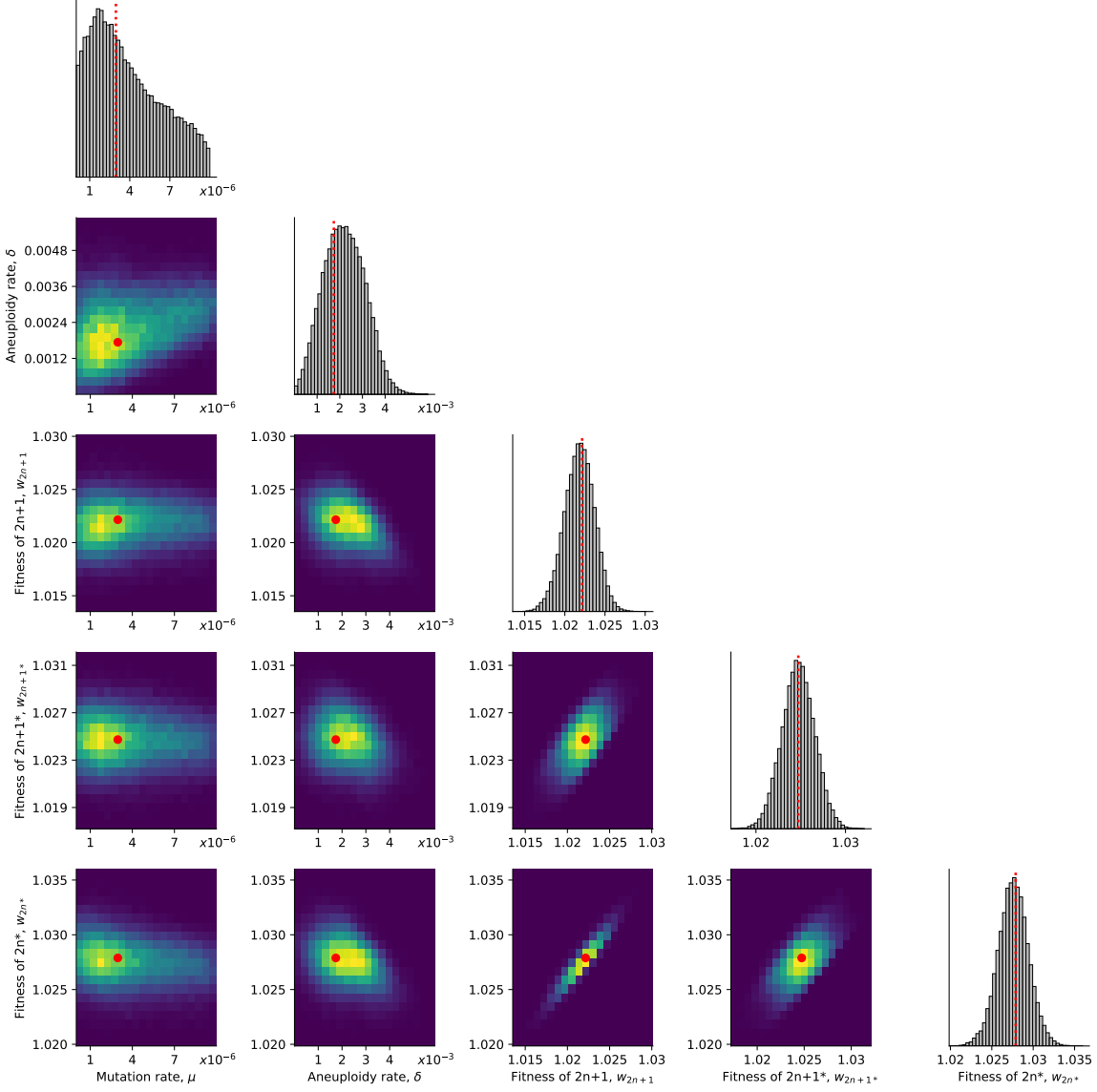


Figure 3: Posterior distribution of model parameters. On the diagonal, the marginal posterior distribution of each model parameter. Below the diagonal, the joint posterior distribution of pairs of model parameters (dark purple and bright yellow for low and high density, respectively). Red markers and orange lines for the joint MAP estimate (which may differ from the marginal MAP, as the marginal distribution integrates over all other parameters).

Model comparison and goodness-of-fit. Our model fits the data well: in simulations using the MAP parameter estimates, $2n^*$ fixed in 61% of simulations by generation 1,700 and in 100% of simulations by generation 2,350 (Figure 4B).

However, a model without aneuploidy (where the aneuploidy rate is fixed at zero, $\delta = 0$), fails to explain the experimental observations (Figure 4). The estimated mutation rate without aneuploidy

is $\mu = 7.98 \cdot 10^{-9}$ [$7.906 \cdot 10^{-9} - 8.138 \cdot 10^{-9}$], much lower compared to a model with aneuploidy and suggesting a target size of just 40. The fitness of the mutant is also much lower at $w_{2n^*} = 1.013$ [1.012 – 1.013]. This is because, without aneuploidy, a high mutation rate or fitness effect will lead to faster appearance and fixation of $2n^*$ than in the experimental observations. Even with these lower estimates, the model fit is worse than that of a model with aneuploidy (Figure 4).

We also checked a model in which aneuploidy occurs but is adaptively neutral compared to the wild-type, that is, $w_{2n+1} = w_{2n}$ and $w_{2n+1^*} = w_{2n^*}$ but $\delta > 0$. This model fits the data better than the model with no aneuploidy (in which $\delta = 0$), but worse than a model with positive selection for aneuploidy, in which $w_{2n} < w_{2n+1} < w_{2n+1^*} < w_{2n^*}$ (Figure 4).

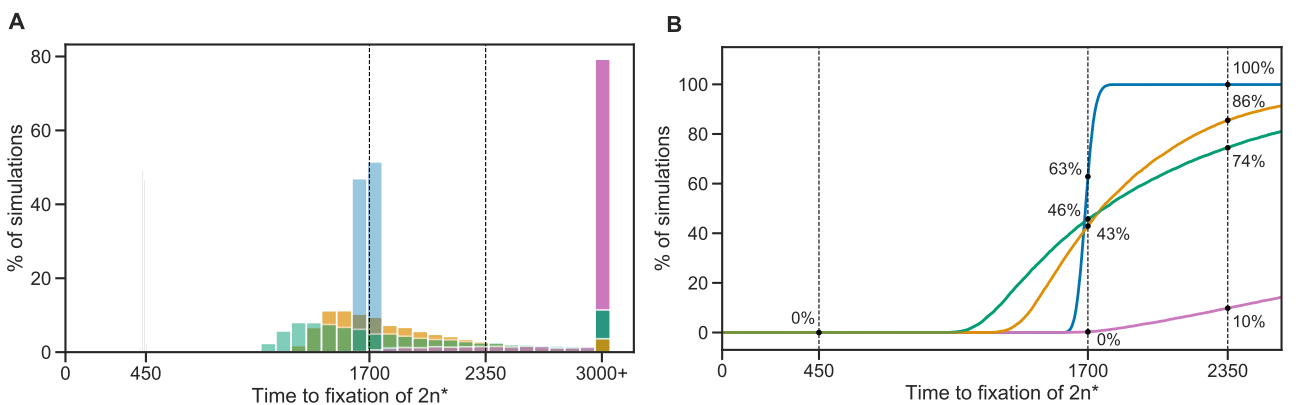


Figure 4: Model fit with and without aneuploidy. The distribution of time to fixation of $2n^*$ (i.e., adaptation time) in 10,000 simulations using MAP parameters of the model with beneficial aneuploidy (blue; $\delta > 0$, $w_{2n} < w_{2n+1} < w_{2n+1^*} < w_{2n^*}$) compared to alternative models: a model with the same parameter values but without aneuploidy (gray, $\delta = 0$, concentrated at $t = 450$); a model fitted to the data assuming no aneuploidy (green, $\delta = 0$); a model fitted to the data assuming neutral aneuploidy (yellow, $\delta > 0$, $w_{2n+1} = w_{2n}$, $w_{2n+1^*} = w_{2n^*}$); and a model with beneficial aneuploidy and an extended prior distribution (pink). In the experiment by Yona et al.⁵¹, one population lost aneuploidy by generation 1,700 and another by generation 2,350 (dashed lines) but not before generation 450. Thus, the blue distribution has a better fit compared to the other distributions (the gray distribution has a particularly poor fit). The MAP likelihood (eq. (4)) is 0.84, 0.78, 0.67, and 0.14 for the models represented by blue, yellow, green, and pink distributions, respectively. **(A)** Histogram of the time to fixation of $2n^*$. The last bin contains all values equal or greater than 3,000. **(B)** Cumulative distribution of the time to fixation.

Model predictions of genotype frequency dynamics. We simulated 50 replicate genotype frequency dynamics using the MAP estimate parameters. Figure 5A shows the simulated frequencies of the four genotypes ($2n$, $2n+1$, $2n+1^*$ and $2n^*$), as well as the frequencies of $2n^*$ cells that arose from

either $2n+1$ cells via a sequences of mutation and chromosome loss events ($2n_A^*$), or directly from $2n$ cells via a mutation event ($2n_M^*$). We find that $2n+1^*$ never reaches substantial frequency as it is quickly replaced by $2n^*$ in a process similar to *stochastic tunneling*^{14,19}.

We tested the *transient adaptive solution hypothesis* by estimating F_A , the expected frequency of $2n^*$ that arose from $2n+1$, computed as the average frequency of such cells at the end of simulations using the MAP estimate parameters. Surprisingly, we observe that the majority of $2n^*$ cells are a product of a direct mutation in $2n$ cells, rather than descending from $2n+1$ cells ($F_A^{MAP} = 0.106$, Figure 5A). This is despite the fact that the $2n+1$ genotype reaches high frequencies in the population (at least 0.98, Figure 5A).

This result is not unique to the MAP parameter estimate. We simulated genotype frequency dynamics using parameter samples from the posterior distribution (Figure 3), and computed the posterior distribution of F_A (Figure 5B). The mean F_A was just 0.1673 [0.0154-0.370 95% CI] and only in 489 of 100,000 posterior samples (0.489%) F_A was larger than 0.5, that is, $2n^*$ was more likely to arise from an aneuploid cell. Thus, if we sample a random cell from the evolved $2n^*$ population, it is more likely to have descended directly from an euploid cell than from an aneuploid cell. The probability of $2n^*$ descending from $2n+1$ (F_A) increases with the aneuploidy rate, δ , and decreases with the mutation rate, μ , and in some cases can also be affected by the fitness parameters (Figure 5C and Figure S9).

Genetic instability in aneuploid cells. It has been suggested that aneuploidy increased genetic instability³⁹. Therefore, we inferred model parameters under the assumption that the mutation rate increases in aneuploid cells by a factor $\tau = 1, 33/32$ (due to an additional chromosome), 2, 5, 10, or 100 (due to genetic instability). We found that the posterior distribution was similar for $\tau = 1, 33/32, 2$, and 5 (Figure S4). With $\tau = 100$, the estimated mutation rate was about 7-8-fold lower compared to $\tau = 1$ ($\mu = 4.094 \cdot 10^{-7}$ [$6.252 \cdot 10^{-8} - 6.046 \cdot 10^{-7}$]) and the aneuploidy rate was about 2-3-fold lower ($\delta = 0.744 \cdot 10^{-3}$ [$0.506 \cdot 10^{-3} - 1.827 \cdot 10^{-3}$]). With $\tau = 10$, the estimated mutation rate was only slightly lower compared to $\tau = 1$ ($\mu = 1.67 \cdot 10^{-6}$ [$2.836 \cdot 10^{-8} - 2.245 \cdot 10^{-6}$]). WAIC (lower is better, see Methods) is lowest for $\tau = 33/32$ and $\tau = 1$ (Table S1). Therefore, evidence does not support an increase in mutation rate in aneuploid cells, and moreover, unless the increase is strong ($\tau \geq 10$), it does not seem to affect our inference. We also checked the differences in genotype frequency dynamics for different τ values. We observe $\tau = 100$ could be distinguished if accurate data was available for the waiting time until the frequency of $2n$ to decrease below 95% (Figure S5A) or for waiting time for the frequency of $2n+1$ to either reach or go below 95% (Figure S5B).

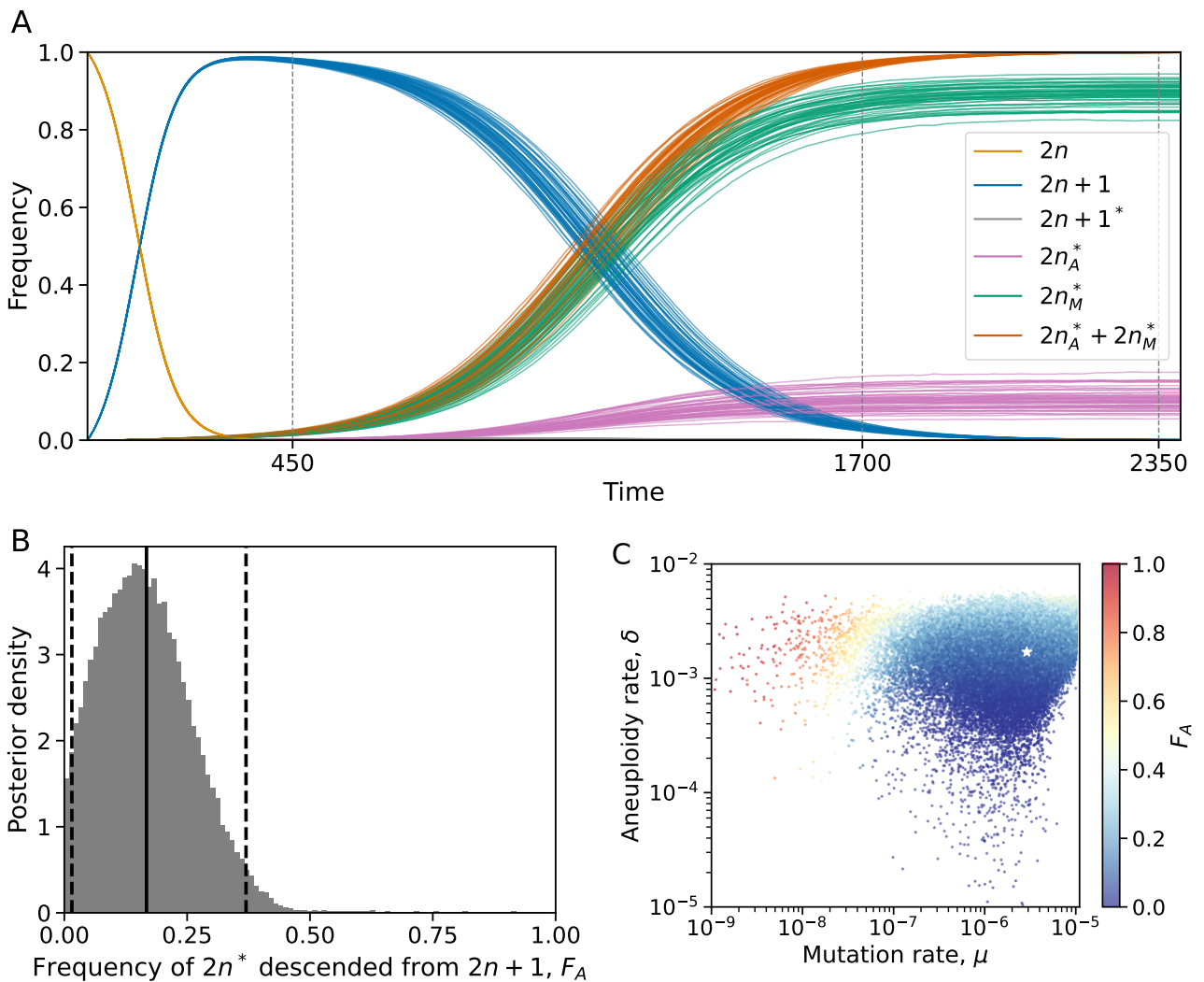


Figure 5: Simulated genotype frequency dynamics. (A) Posterior predicted genotype frequencies over time, including the source of $2n^*$: $2n_A^*$ arose from $2n + 1$, whereas $2n_M^*$ arose directly from $2n$. Shown are 50 simulations using the MAP estimate parameters. (B) Posterior distribution of F_A , the expected frequency of $2n^*$ cells descended from $2n+1$ cells, computed as the average frequency at the end of 100 simulations for 100,000 samples from the parameter posterior distribution. Solid and dashed lines show the mean and 95% CI. (C) F_A values (color coded) from panel B, with their corresponding mutation rate μ on x-axis and aneuploidy rate δ on the y-axis. White star shows the MAP estimate. See also Figure S9.

Discussion

Yona et al.⁵¹ have suggested that the aneuploid cells that come to dominate the experimental populations were later replaced by “refined strains, which eliminated the cost associated with the trisomy, exhibit improved growth both at the permissive and the high temperatures compared with their trisomic ancestors” and that “it is expected that the original contribution of trisomy to heat tolerance was replaced by alternative solutions.”. However, our results suggest that most of the cells in the evolved euploid population do not carry mutations that were common in the aneuploid populations, but rather

a different set of mutations. Therefore, the majority of the evolved euploid cells are not descended from aneuploid cells, but rather are direct descendants of the ancestral population.

⁵¹ have analyzed the expression levels of 14 heat-shock proteins (HSP). They found that their expression level changed “very modestly” in the aneuploid populations, but that most of them “showed significant up-regulation” in the evolved euploid population.

We inferred the rates and fitness effects of aneuploidy and mutation in a previously published evolutionary experiment in which yeast populations adapted to heat stress⁵¹. We estimate that the aneuploidy rate (i.e., number of chromosome gains per generation) is $1.7 \cdot 10^{-3}$, is higher than a previous estimate of $6.7 \cdot 10^{-6}$ ⁵³. We find no evidence for increased mutation rates in aneuploid cells.

Conclusions.

Models and Methods

DNA sequencing.

Evolutionary genetic model. We model the evolution of a population of cells using a Wright-Fisher model²⁶, assuming a constant effective population size N , non-overlapping generations, and including the effects of natural selection, genetic drift, aneuploidy, and mutation. We focus on beneficial genetic modifications, neglecting the effects of deleterious and neutral mutations or karyotypic changes. The model allows for a single aneuploid karyotype (e.g., chromosome III duplication) and a single mutation to accumulate in the genotype. Thus, the model follows four genotypes (Figure 2): euploid wild-type, $2n$, the initial genotype; euploid mutant, $2n^*$, with the standard karyotype and a single beneficial mutation; aneuploid wild-type, $2n+1$, with an extra chromosome, i.e., following chromosome duplication; and aneuploid mutant, $2n+1^*$, with an extra chromosome and a beneficial mutation.

Transitions between the genotypes occur as follows (Figure 2): Beneficial mutations from $2n$ to $2n^*$ and from $2n+1$ to $2n+1^*$ occur with probability μ , the mutation rate. We neglect back-mutations (i.e., from $2n^*$ to $2n$ and from $2n+1^*$ to $2n+1$). Aneuploidy is formed by chromosome mis-segregation, so that cells transition from $2n$ to $2n+1$ and from $2n+1^*$ to $2n^*$ with probability δ , the aneuploidy rate. That is, we assume chromosomes are gained and lost at the same rate, and we neglect events that form a less-fit genotype (i.e., $2n+1$ to $2n$ and $2n^*$ to $2n+1^*$).

In the experiment by Yona et al.⁵¹, the population was grown every day from $1.6 \cdot 10^6$ cells until reaching stationary phase and then diluted 1:120. Thus, we set the population size to $N = 6.425 \cdot 10^6$, the harmonic mean of $\{2^k \cdot 1.6 \cdot 10^6\}_{k=0}^7$ ⁶. The initial population has N cells with genotype $2n$. The effect of natural selection on the frequency f_i of genotype $i = 2n, 2n + 1, 2n + 1^*$, or $2n^*$ is given by

$$f_i^s = \frac{f_i w_i}{\bar{w}}, \quad (1)$$

where w_i is the fitness of genotype i and $\bar{w} = \sum_j f_j w_j$ is the population mean fitness. The effect of mutation and aneuploidy on genotype frequencies is given by

$$\begin{aligned} f_{2n}^m &= (1 - \delta - \mu) f_{2n}^s, \\ f_{2n+1}^m &= \delta f_{2n}^s + (1 - \mu) f_{2n+1}^s, \\ f_{2n+1^*}^m &= \mu f_{2n+1}^s + (1 - \delta) f_{2n+1^*}^s, \\ f_{2n^*}^m &= \mu f_{2n}^s + \delta f_{2n+1}^s + f_{2n^*}^s. \end{aligned} \quad (2)$$

Finally, random genetic drift is modeled using a multinomial distribution²⁶,

$$\mathbf{f}' \sim \frac{1}{N} \cdot \text{Mult}(N, \mathbf{f}^m), \quad (3)$$

where $\mathbf{f}^m = (f_{2n}^m, f_{2n+1}^m, f_{2n+1^*}^m, f_{2n^*}^m)$ are the frequencies of the genotypes after mutation and aneuploidy, \mathbf{f}' are the genotype frequencies in the next generation, and $\text{Mult}(N, \mathbf{f})$ is a multinomial distribution parameterized by the population size N and the genotype frequencies \mathbf{f} . Overall, the change in genotype frequencies from one generation to the next is given by the transformation $f_i \rightarrow f'_i$.

Empirical data for model inference. We use the results of evolutionary experiments reported by Yona et al.⁵¹. In their heat-stress experiment, four populations of *S. cerevisiae* evolved under 39 °C. Aneuploidy fixed in all four population in the first 450 generations (hereafter, fixation or elimination of a genotype *by generation t* means that more than 95% or less than 5% of the population carry the genotype at generation t , and possibly earlier). From re-analysis of data not published in the original paper, aneuploidy did not fix before at least 200 generations elapsed. The experiment continued with two populations, in which aneuploidy was eliminated by generation 1,700 and 2,350 while still under the same conditions of elevated heat (39 °C).

Likelihood function. Because our model, just like the Wright-Fisher model, is non-linear and stochastic, computing the distribution of fixation time $T(g)$ of genotype g for use in the likelihood function is intractable (it is even hard to use a diffusion-equation approximation due to the model having

multiple genotypes, rather than just two). We overcome this problem by approximating the likelihood using simulations. We simulate 1,000 experiments per parameter vector $\theta = (\mu, \delta, s, b, c)$, resulting in a set of simulated observations $\tilde{\mathbf{X}} = \{\tilde{X}_i\}_{i=1}^{1000}$. We then compute the approximate likelihood,

$$\begin{aligned}\mathcal{L}(\theta) = P^4(200 \leq T(2n+1) \leq 450) \cdot & \left[1 - \right. \\ & P_{\tilde{\mathbf{X}}}^4(\{\{T(2n^*) < 1700\} \mid 200 \leq T(2n+1) \leq 450\}) - \\ & P_{\tilde{\mathbf{X}}}^4(\{\{1700 < T(2n^*) < 2350\} \mid 200 \leq T(2n+1) \leq 450\}) + \\ & \left. P_{\tilde{\mathbf{X}}}^4(\{\{T(2n^*) < 1700\} \wedge \{\{1700 < T(2n^*) < 2350\} \mid 200 \leq T(2n+1) \leq 450\}) \right],\end{aligned}\tag{4}$$

where $!\{\dots\}$ is the "logical not" operator, $P^4(\dots)$ is the 4th power of $P(\dots)$, and all probabilities $P_{\tilde{\mathbf{X}}}(\dots)$ are approximated from the results of the simulations $\tilde{\mathbf{X}}$. For example, $P_{\tilde{\mathbf{X}}}(\{\{T(2n^*) < 1700\} \mid 200 \leq T(2n+1) \leq 450\})$ is approximated by taking simulations in which $2n+1$ fixed before generation 450 but not before generation 200, and computing the fraction of such simulations in which $2n^*$ did not fix by generation 1,700, and hence aneuploidy did not extinct before generation 1,700. Figure S1 compares results with less and more simulated experiments, demonstrating that 1,000 simulations are likely sufficient.

For a model without aneuploidy (that is, when the aneuploidy rate is fixed at zero, $\delta = 0$), we disregard the increased expression in chromosome III and the growth advantage measured in generation 450, and focus on the growth advantage measured in later generations, presumably due to a beneficial mutation. Therefore, the likelihood is approximated by

$$\begin{aligned}\mathcal{L}_!(\theta) = 1 - & P_{\tilde{\mathbf{X}}}^4(\{\{T(2n^*) < 1700\}\}) - \\ & P_{\tilde{\mathbf{X}}}^4(\{\{1700 < T(2n^*) < 2350\}\}) + \\ & P_{\tilde{\mathbf{X}}}^4(\{\{T(2n^*) < 1700\} \wedge \{\{1700 < T(2n^*) < 2350\}\}).\end{aligned}\tag{5}$$

Parameter inference. To infer model parameters, we use approximate Bayesian computation with a sequential Monte-Carlo scheme, or ABC-SMC⁴², implemented in the pyABC Python package¹⁸ pyabc.readthedocs.io. This approach uses numerical stochastic simulations of the model to infer a posterior distribution over the model parameters. It is a method of likelihood-free, simulation-based inference⁵, that is, for estimating a posterior distribution when a likelihood function cannot be directly computed. It is therefore suitable in our case, in which the likelihood function can only be approximated from simulations, and cannot be directly computed.

The ABC-SMC algorithm employs sequential importance sampling over multiple iterations^{45,17,43}. In iteration t of the algorithm, a set of parameter vectors, $\{\theta_{i,t}\}_{i=1}^{n_t}$, also called *particles*, are constructed

in the following way. A proposal particle, θ^* , is sampled from a proposal distribution, and is either accepted or rejected, until n_t particles are accepted. The number of particles, n_t , is adapted at every iteration t using the adaptive population strategy¹⁸ pyabc.readthedocs.io. For $t = 0$, the proposal particle is sampled from the prior distribution, $p(\theta)$. For $t > 0$, the proposal particle is sampled from the particles accepted in the previous iteration, $\{\theta_{i,t-1}\}_{i=1}^{n_{t-1}}$, each with a probability relative to its weight $W_{t-1}(\theta_{i,t-1})$ (see below). The proposal particle is then perturbed using a kernel perturbation kernel, $K_t(\theta^* \mid \theta)$ where θ is the sample from the previous iteration. Then, a set of synthetic observations $\tilde{\mathbf{X}}^*$ is simulated, and the proposal particle θ^* is accepted if its approximate likelihood (eq. (4)) is high enough, $\mathcal{L}(\theta^*) > 1 - \epsilon_t$ (or more commonly, if $1 - \mathcal{L}(\theta^*) < \epsilon_t$), where $\epsilon_t > 0$ is the *acceptance threshold*, as higher values of ϵ_t allow more particles to be accepted. The acceptance threshold ϵ_t is chosen as the median of the $1 - \mathcal{L}(\theta)$ of the particles accepted in the previous iteration, $t - 1$, and $\epsilon_0 = 0.01$. For each accepted particle $\theta_{i,t}$ a weight $W_t(\theta_{i,t})$ is assigned: for $t = 0$, $W_0(\theta_{i,0}) = 1$, and for $t > 0$, $W_t(\theta_{i,t}) = p(\theta_{i,t}) / \sum_{i=1}^{n_{t-1}} W_{t-1}(\theta_{i,t-1}) K_t(\theta_{i,t}, \theta_{i,t-1})$, where $p(\theta)$ is the prior density of θ and $K_t(\theta', \theta)$ is the probability of a perturbation from θ to θ' . $K_t(\theta' \mid \theta)$ is a multivariate normal distribution, fitted at iteration t to the particles from the previous iteration, $\{\theta_{i,t-1}\}_{i=1}^{n_{t-1}}$, and their weights, $\{W(\theta_{i,t-1})\}_{i=1}^{n_{t-1}}$.

Acceptance is determined according to the approximate likelihood (eq. (4)), which has a maximum value of $\mathcal{L}_{max} = 0.875$ (giving a minimal value of $\epsilon_{min} = 0.125$). We terminated the inference iterations when the change in ϵ value from one iteration to the next was small. With our standard prior and model, we reached $\epsilon = 0.13$ (or $\mathcal{L} = 0.87$) after six iterations, with $n_6 = 982$ accepted parameter vectors and effective sample size ESS=651 (Figure S2). Running the inference algorithm with different initialization seeds and less or more simulations for approximating the likelihood produced similar posterior distributions (Figure S1).

After producing a set of weighted particles from the the posterior distribution using the above ABC-SMC algorithm, we approximate the posterior using kernel density estimation (KDE) with Gaussian kernels. We truncate the estimated posterior to avoid positive posterior density for values with zero prior density. The MAP (maximum a posteriori) estimate is computed as the the maximum of the estimated joint posterior density. We then draw 5,000,000 samples from the posterior distribution to compute the HDI (highest density interval) and draw 50,000 samples to visualize the posterior distribution with histograms.

Model comparison. We examine several versions of our evolutionary models, e.g. without aneuploidy or with increased mutation rate in aneuploid cells, as well as several different prior distributions

(see below). To compare these, we plot posterior predictions: for each model we execute 10,000 simulations using the MAP parameter estimates and plot the distributions of time to fixation of $2n^*$, one of key properties of the model likelihood. These plots visualize the fit of each model to the data. Also, for similar models we plot the marginal and joint posterior distributions of the parameters; if these are similar, we consider the models interchangeable. We validate this by comparing HDI (highest density interval) of posterior distributions.

Where posterior plots are very similar and the number of parameters is the same, we use WAIC, or the widely applicable information criterion⁹, defined as

$$WAIC(\theta) = -2 \log \mathbb{E}[\mathcal{L}(\theta)] + 2\mathbb{V}[\log \mathcal{L}(\theta)] \quad (6)$$

where θ is a parameter vector, and $\mathbb{E}[\cdot]$ and $\mathbb{V}[\cdot]$ are the expectation and variance taken over the posterior distribution, which in practice are approximated using 50,000 samples from the posterior KDE. We validated that upon resampling WAIC values do not significantly change and that differences in WAIC between models are preserved. WAIC values are scaled as a deviance measure: lower values imply higher predictive accuracy¹⁵.

Prior distributions. We used informative prior distributions for $w_{2n+1} = 1 - c + b$, $w_{2n+1^*} = (1+s)(1-c)+b$ and $w_{2n^*} = 1+s$, which we estimated from growth curves data from mono-culture growth experiments previously reported by Yona et al.⁵¹, Figs. 3C, 4A, and S2. We used Curveball, a method for predicting results of competition experiments from growth curve data²⁸ curveball.yoavram.com. Briefly, Curveball takes growth curves of two strains growing separately in mono-culture and predicts how they would grow in a mixed culture, that is, it predicts the results of a competition assay. From these predictions, relative fitness values can be computed. Because Curveball uses a maximum-likelihood approach to estimate model parameters, we were able to estimate a distribution of relative fitness values to be used as a prior distribution by sampling 10,000 samples from a truncated multivariate normal distribution defined by the maximum-likelihood covariance matrix (Figure S3).

We used growth curves of $2n$ and $2n+1$ in 39 °C to estimate an informative prior distribution for w_{2n+1} (Figure S3-D, assuming $w_{2n} = 1$). In this prior distribution, we used the same prior for w_{2n+1^*} and w_{2n^*} . To increase computational efficiency, we also assumed $w_{2n^*} > w_{2n+1^*} > w_{2n+1} > w_{2n}$; running the inference without this assumption produced similar results. See *supporting material* for an extended informative prior distribution that uses growth curves of $2n^*$ and $2n+1$ growing in 39 °C; this prior distribution proved to be less useful.

As a control, we tested an uninformative uniform prior with $U(1, 6)$, for (i) all w_{2n+1} , w_{2n+1^*} , w_{2n^*} , or

(ii) only for w_{2n+1*} , w_{2n*} , using the above informative prior for w_{2n+1} . In these cases the inference algorithm failed to converge.

For the mutation rate, μ , and aneuploidy rate, δ , we used uninformative uniform priors, $\mu \sim U(10^{-9}, 10^{-5})$ and $\delta \sim U(10^{-6}, 10^{-2})$. A wider mutation rate prior, $\mu \sim U(10^{-9}, 10^{-3})$, produced similar results.

Acknowledgements

We thank Yitzhak Pilpel, Orna Dahan, Lilach Hadany, Judith Berman, David Gresham, Shay Covo, Martin Kupiec, Uri Obolski, and Tal Simon for discussions and comments. This work was supported in part by the Israel Science Foundation (ISF, YR 552/19), the US–Israel Binational Science Foundation (BSF, YR 2021276) Minerva Stiftung center for Lab Evolution (YR), Minerva Stiftung short-term research grant (MP).

References

- [1] Avecilla, G., Chuong, J. N., Li, F., Sherlock, G., Gresham, D. and Ram, Y. 2022, ‘Neural networks enable efficient and accurate simulation-based inference of evolutionary parameters from adaptation dynamics’, *PLOS Biol.* **20**(5), e3001633.
- [2] Bakhoum, S. F. and Landau, D. A. 2017, ‘Chromosomal instability as a driver of tumor heterogeneity and evolution’, *Cold Spring Harb. Perspect. Med.* **7**(6), 1–14.
- [3] Boveri, T. 2008, ‘Concerning the Origin of Malignant Tumours’, *J. Cell Sci.* **121**(Supplement 1), 1–84.
- [4] Covo, S., Puccia, C. M., Argueso, J. L., Gordenin, D. A. and Resnick, M. A. 2014, ‘The sister chromatid cohesion pathway suppresses multiple chromosome gain and chromosome amplification.’, *Genetics* **196**(2), 373–384.
- [5] Cranmer, K., Brehmer, J. and Louppe, G. 2020, ‘The frontier of simulation-based inference’, *Proc. Natl. Acad. Sci. U. S. A.* p. 201912789.
- [6] Crow, J. F. and Kimura, M. 1970, *An introduction to population genetics theory*, Burgess Pub. Co., Minneapolis.
- [7] Dhar, R., Sägesser, R., Weikert, C., Yuan, J. and Wagner, A. 2011, ‘Adaptation of *Saccharomyces cerevisiae* to saline stress through laboratory evolution.’, *J. Evol. Biol.* **24**(5), 1135–53.

- [8] Dunham, M. J., Badrane, H., Ferea, T., Adams, J., Brown, P. O., Rosenzweig, F. and Botstein, D. 2002, ‘Characteristic genome rearrangements in experimental evolution of *Saccharomyces cerevisiae*’, *Proc. Natl. Acad. Sci.* **99**(25), 16144–16149.
- [9] Gelman, A., Carlin, J. B., Stern, H. S., Dunson, D. B., Vehtari, A. and Rubin, D. B. 2013, *Bayesian Data Analysis, Third Edition*, Chapman & Hall/CRC Texts in Statistical Science, Taylor & Francis.
- [10] Gerstein, A. C. and Berman, J. 2018, ‘Diversity of acquired adaptation to fluconazole is influenced by genetic background and ancestral fitness in *Candida albicans*’, *bioRxiv* p. 360347.
- [11] Gerstein, A. C., Ono, J., Lo, D. S., Campbell, M. L., Kuzmin, A. and Otto, S. P. 2015, ‘Too much of a good thing: the unique and repeated paths toward copper adaptation.’, *Genetics* **199**(2), 555–71.
- [12] Gresham, D., Desai, M. M., Tucker, C. M., Jenq, H. T., Pai, D. A., Ward, A., DeSevo, C. G., Botstein, D. and Dunham, M. J. 2008, ‘The repertoire and dynamics of evolutionary adaptations to controlled nutrient-limited environments in yeast’, *PLoS Genet.* **4**(12).
- [13] Hong, J. and Gresham, D. 2014, ‘Molecular Specificity, Convergence and Constraint Shape Adaptive Evolution in Nutrient-Poor Environments’, *PLoS Genet.* **10**(1).
- [14] Iwasa, Y., Michor, F. and Nowak, M. A. 2004, ‘Stochastic Tunnels in Evolutionary Dynamics’, *Genetics* **166**(3), 1571–1579.
- [15] Kass, R. E. and Raftery, A. E. 1995, ‘Bayes Factors’, *J. Am. Stat. Assoc.* **90**(430), 773.
- [16] Kasuga, T., Bui, M., Bernhardt, E., Swiecki, T., Aram, K., Cano, L. M., Webber, J., Brasier, C., Press, C., Grünwald, N. J., Rizzo, D. M. and Garbelotto, M. 2016, ‘Host-induced aneuploidy and phenotypic diversification in the Sudden Oak Death pathogen *Phytophthora ramorum*’, *BMC Genomics* **17**(1), 1–17.
- [17] Klinger, E. and Hasenauer, J. 2017, A Scheme for Adaptive Selection of Population Sizes in Approximate Bayesian Computation - Sequential Monte Carlo, in J. Feret and H. Koepll, eds, ‘Computational Methods in Systems Biology’, Vol. 10545, Springer International Publishing, pp. 128–144. Series Title: Lecture Notes in Computer Science.
- [18] Klinger, E., Rickert, D. and Hasenauer, J. 2018, ‘pyABC: distributed, likelihood-free inference’, *Bioinformatics* (May), 1–3.
- [19] Komarova, N. L., Sengupta, A. and Nowak, M. A. 2003, ‘Mutation-selection networks of cancer

- initiation: Tumor suppressor genes and chromosomal instability’, *J. Theor. Biol.* **223**(4), 433–450.
- [20] Kumaran, R., Yang, S.-Y. and Leu, J.-Y. 2013, ‘Characterization of chromosome stability in diploid, polyploid and hybrid yeast cells’, **8**(7), e68094.
- [21] Lynch, M., Sung, W., Morris, K., Coffey, N., Landry, C. R., Dopman, E. B., Dickinson, W. J., Okamoto, K., Kulkarni, S., Hartl, D. L. and Thomas, W. K. 2008, ‘A genome-wide view of the spectrum of spontaneous mutations in yeast’, **105**(27), 9272–9277.
- [22] Mannaert, A., Downing, T., Imamura, H. and Dujardin, J. C. 2012, ‘Adaptive mechanisms in pathogens: Universal aneuploidy in *Leishmania*’, *Trends Parasitol.* **28**(9), 370–376.
- [23] Möller, M., Habig, M., Freitag, M. and Stukenbrock, E. H. 2018, ‘Extraordinary Genome Instability and Widespread Chromosome Rearrangements During Vegetative Growth’, *Genetics* **210**(2), 517–529.
- [24] Naylor, R. M. and van Deursen, J. M. 2016, ‘Aneuploidy in Cancer and Aging’, *Annu. Rev. Genet.* **50**(1), 45–66.
- [25] Niwa, O., Tange, Y. and Kurabayashi, A. 2006, ‘Growth arrest and chromosome instability in aneuploid yeast’, *Yeast* **23**(13), 937–950.
- [26] Otto, S. P. and Day, T. 2007, *A biologist’s guide to mathematical modeling in ecology and evolution*, Princeton University Press.
- [27] Pavelka, N., Rancati, G., Zhu, J., Bradford, W. D., Saraf, A., Florens, L., Sanderson, B. W., Hattem, G. L. and Li, R. 2010, ‘Aneuploidy confers quantitative proteome changes and phenotypic variation in budding yeast.’, *Nature* **468**(7321), 321–5.
- [28] Ram, Y., Dellus-Gur, E., Bibi, M., Karkare, K., Obolski, U., Feldman, M. W., Cooper, T. F., Berman, J. and Hadany, L. 2019, ‘Predicting microbial growth in a mixed culture from growth curve data’, *Proc. Natl. Acad. Sci. U. S. A.* **116**(29), 14698–14707.
- [29] Rancati, G., Pavelka, N., Fleharty, B., Noll, A., Trimble, R., Walton, K., Perera, A., Staehling-Hampton, K., Seidel, C. W. and Li, R. 2008, ‘Aneuploidy Underlies Rapid Adaptive Evolution of Yeast Cells Deprived of a Conserved Cytokinesis Motor’, *Cell* **135**(5), 879–893.
- [30] Robbins, N., Caplan, T. and Cowen, L. E. 2017, ‘Molecular Evolution of Antifungal Drug Resistance’, *Annu. Rev. Microbiol.* **71**(1), 753–775.

- [31] Rodrigues, M. L. and Albuquerque, P. C. 2018, ‘Searching for a change: The need for increased support for public health and research on fungal diseases’, *PLoS Negl. Trop. Dis.* **12**(6), 1–5.
- [32] Santaguida, S. and Amon, A. 2015, ‘Short- and long-term effects of chromosome mis-segregation and aneuploidy’, *Nat. Rev. Mol. Cell Biol.* **16**(8), 473–485.
- [33] Santaguida, S., Vasile, E., White, E. and Amon, A. 2015, ‘Aneuploidy-induced cellular stresses limit autophagic degradation’, *Genes Dev.* **29**(19), 2010–2021.
- [34] Schvartzman, J. M., Sotillo, R. and Benezra, R. 2010, ‘Mitotic chromosomal instability and cancer: Mouse modelling of the human disease’, *Nat. Rev. Cancer* **10**(2), 102–115.
- [35] Selmecki, A. M., Dulmage, K., Cowen, L. E., Anderson, J. B. and Berman, J. 2009, ‘Acquisition of Aneuploidy Provides Increased Fitness during the Evolution of Antifungal Drug Resistance’, *PLoS Genet.* **5**(10), e1000705.
- [36] Selmecki, A. M., Forche, A. and Berman, J. 2010, ‘Genomic Plasticity of the Human Fungal Pathogen *Candida albicans*’, *Eukaryot. Cell* **9**(7), 991–1008.
- [37] Selmecki, A. M., Gerami-Nejad, M., Paulson, C., Forche, A. and Berman, J. 2008, ‘An isochromosome confers drug resistance in vivo by amplification of two genes, ERG11 and TAC1’, *Mol. Microbiol.* **68**(3), 624–641.
- [38] Sheltzer, J. M. and Amon, A. 2011, ‘The aneuploidy paradox: Costs and benefits of an incorrect karyotype’, *Trends Genet.* **27**(11), 446–453.
- [39] Sheltzer, J. M., Blank, H. M., Pfau, S. J., Tange, Y., George, B. M., Humpton, T. J., Brito, I. L., Hiraoka, Y., Niwa, O. and Amon, A. 2011, ‘Aneuploidy Drives Genomic Instability in Yeast’, *Science (80-.).* **333**(6045), 1026–1030.
- [40] Sheltzer, J. M., Ko, J. H., Replogle, J. M., Habibe Burgos, N. C., Chung, E. S., Meehl, C. M., Sayles, N. M., Passerini, V., Storchova, Z. and Amon, A. 2017, ‘Single-chromosome Gains Commonly Function as Tumor Suppressors’, *Cancer Cell* **31**(2), 240–255.
- [41] Sionov, E., Lee, H., Chang, Y. C. and Kwon-Chung, K. J. 2010, ‘*Cryptococcus neoformans* Overcomes Stress of Azole Drugs by Formation of Disomy in Specific Multiple Chromosomes’, *PLoS Pathog.* **6**(4), e1000848.
- [42] Sisson, S. A., Fan, Y. and Tanaka, M. M. 2007, ‘Sequential Monte Carlo without likelihoods’, *Proc. Natl. Acad. Sci.* **104**(6), 1760–1765.

- [43] Syga, S., David-Rus, D., Schälte, Y., Hatzikirou, H. and Deutsch, A. 2021, ‘Inferring the effect of interventions on COVID-19 transmission networks’, *Sci. Rep.* **11**(1), 1–11.
- [44] Todd, R. T., Forche, A. and Selmecki, A. M. 2017, ‘Ploidy Variation in Fungi: Polyploidy, Aneuploidy, and Genome Evolution’, *Microbiol. Spectr.* **5**(4), 1–20.
- [45] Toni, T., Welch, D., Strelkowa, N., Ipsen, A. and Stumpf, M. P. 2009, ‘Approximate Bayesian computation scheme for parameter inference and model selection in dynamical systems’, *J. R. Soc. Interface* **6**(31), 187–202.
- [46] Torres, E. M., Dephoure, N., Panneerselvam, A., Tucker, C. M., Whittaker, C. A., Gygi, S. P., Dunham, M. J. and Amon, A. 2010, ‘Identification of aneuploidy-tolerating mutations’, *Cell* **143**(1), 71–83.
- [47] Torres, E. M., Sokolsky, T., Tucker, C. M., Chan, L. Y., Boselli, M., Dunham, M. J. and Amon, A. 2007, ‘Effects of Aneuploidy on Cellular Physiology and Cell Division in Haploid Yeast’, *Science (80-.).* **317**(5840), 916–924.
- [48] Tsai, H. J., Nelliat, A. R., Choudhury, M. I., Kucharavy, A., Bradford, W. D., Cook, M. E., Kim, J., Mair, D. B., Sun, S. X., Schatz, M. C. and Li, R. 2019, ‘Hypo-osmotic-like stress underlies general cellular defects of aneuploidy’, *Nature* .
- [49] Williams, B. R., Prabhu, V. R., Hunter, K. E., Glazier, C. M., Whittaker, C. a., Housman, D. E. and Amon, A. 2008, ‘Aneuploidy Affects Proliferation and Spontaneous Immortalization in Mammalian Cells’, *Science (80-.).* **322**(5902), 703–709.
- [50] Yang, F., Todd, R. T., Selmecki, A., Jiang, Y. Y., Cao, Y. B. and Berman, J. 2021, ‘The fitness costs and benefits of trisomy of each *Candida albicans* chromosome’, *Genetics* **218**(2), 1–7.
- [51] Yona, A., Manor, Y. S., Herbst, R. H., Romano, G. H., Mitchell, A., Kupiec, M., Pilpel, Y. and Dahan, O. 2012, ‘Chromosomal duplication is a transient evolutionary solution to stress.’, *Proc. Natl. Acad. Sci.* **109**(51), 21010–5.
- [52] Zhu, J., Tsai, H.-J., Gordon, M. R. and Li, R. 2018, ‘Cellular Stress Associated with Aneuploidy’, *Dev. Cell* **44**(4), 420–431.
- [53] Zhu, Y. O., Sherlock, G. and Petrov, D. A. 2016, ‘Whole Genome Analysis of 132 Clinical *Saccharomyces cerevisiae* Strains Reveals Extensive Ploidy Variation’, *G3 Genes, Genomes, Genet.* **6**(8), 2421–2434.

- [54] Zhu, Y. O., Siegal, M. L., Hall, D. W. and Petrov, D. A. 2014, ‘Precise estimates of mutation rate and spectrum in yeast’, **111**(22), E2310–E2318.

Supplementary Material

Supplementary Analysis

Sensitivity analysis. Changing a single parameter while keeping the rest fixed at the MAP estimate produces a worse fit to the data (Figure S6). Furthermore, we fitted models with a mutation rate fixed at $\mu=10^{-5}$, 10^{-6} and 10^{-7} . We inferred similar parameters estimates for the model with $\mu = 10^{-6}$ compared to the model with a free μ parameter, in which the inferred mutation rate is $\mu \approx 3 \cdot 10^{-6}$. Models with $\mu=10^{-5}$ and $\mu=10^{-7}$ inferred different parameters estimates, including higher aneuploidy rate and lower fitness values for $2n+1$ and $2n^*$ (Figure S7).

Extended informative prior distribution. In an extended informative prior distribution, we used additional growth curves of $2n^*$ (*refined* strain from Yona et al.⁵¹) and $2n+1$ in 39 °C to estimate w_{2n^*}/w_{2n+1} (Figure S3L). The same distribution was used for w_{2n^*}/w_{2n+1*} . Thus, our main informative prior uses a single prior distribution for fitness values of $2n+1$, $2n+1^*$, and $2n^*$, whereas the extended informative prior uses one distribution for $2n+1$, and another distribution for both $2n+1^*$ and $2n^*$.

We estimated the parameters under this extended informative prior. Inference took much longer to run but the posterior distribution seemed to converge, as it did not change much in the final iterations. The posterior predictive plot shows that inference with this extended prior produces a posterior distribution that fails to explain the empirical observations (pink in Figure 4). However, the inferred posterior distribution is considerably narrower (compare Figures 3 and S8) and therefore parameter estimates are less variable. The estimated mutation rate was much lower compared to the main informative prior, with $\mu = 2.475 \cdot 10^{-9}$ [$2.419 \cdot 10^{-9} - 2.609 \cdot 10^{-9}$]. Other parameter estimates are: $\delta = 2.707 \cdot 10^{-3}$ [$2.093 \cdot 10^{-3} - 3.092 \cdot 10^{-3}$], $w_{2n+1} = 1.022$ [$1.021 - 1.024$], $w_{2n+1*} = 1.029$ [$1.027 - 1.03$], $w_{2n^*} = 1.03$ [$1.029 - 1.031$]. Notably, the maximum posterior ratio $w_{2n^*}/w_{2n+1} = 1.007$ is much lower than the maximum prior ratio of 1.033 (Figure S3H) and closer to the ratio of 1 that we assume in our standard prior. Together with the posterior predictive results, we conclude that the main informative prior is preferable over the extended informative prior.

Supplementary Figures & Tables

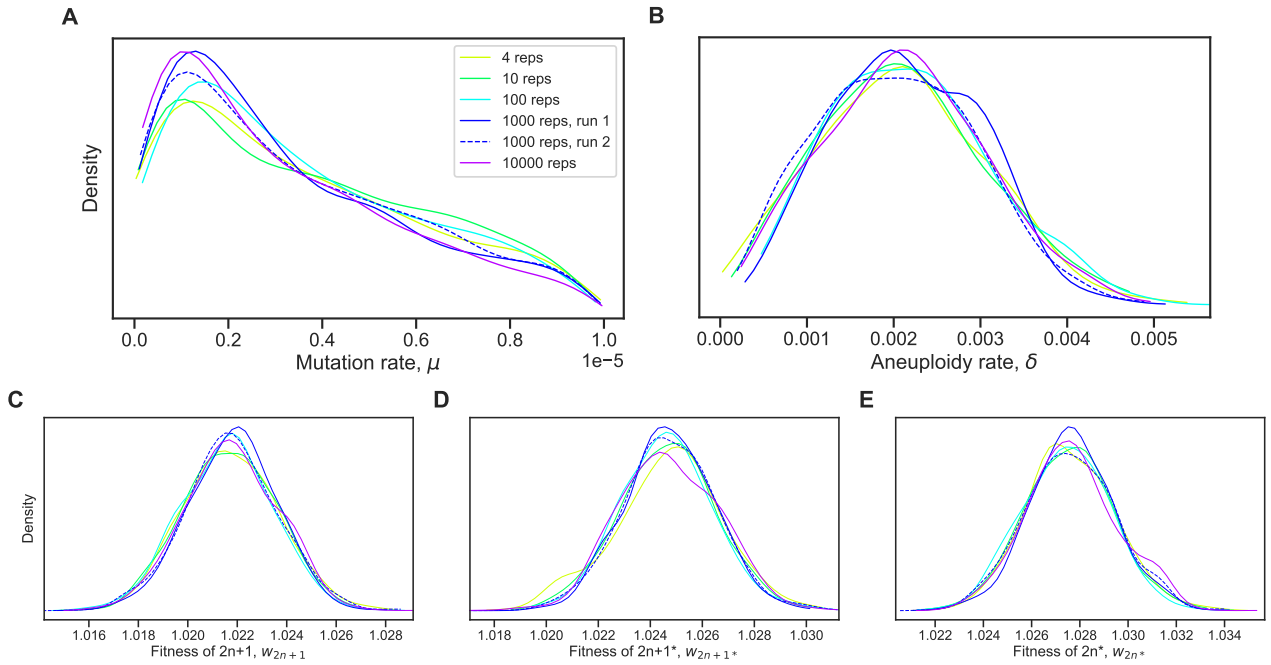


Figure S1: Posterior distribution validation. The posterior distribution of model parameters is roughly the same regardless of the number of simulations (4-10,000 replicates) used to approximate the likelihood (eq. (4)).

Table S1: WAIC values for different τ values.

Model	WAIC
$\tau = 1$	295
$\tau = 33/32$	266
$\tau = 2$	501
$\tau = 5$	376
$\tau = 10$	318
$\tau = 100$	319

WAIC defined in eq. (6).

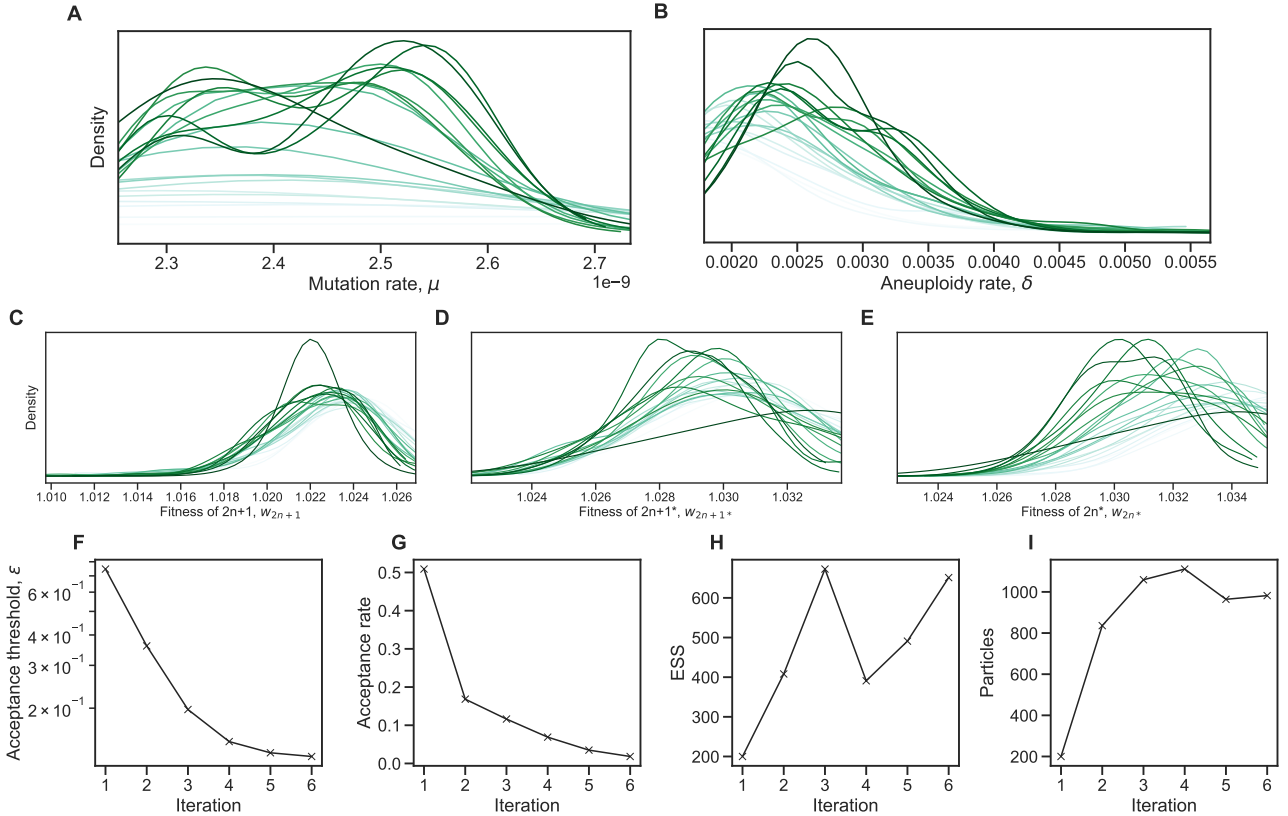


Figure S2: Inference convergence. The ABC-SMC algorithm was used to infer the model parameters. **(A-E)** The approximate posterior distributions of model parameters at each iteration of the ABC-SMC algorithm demonstrates convergence, as the posterior did not significantly change after the first iteration, $t = 1$. **(F-I)** ABC-SMC measures of convergence. After iteration number 6, the acceptance threshold was $\epsilon = 0.13$ (i.e., $\mathcal{L} = 0.87$, eq. (4)), the acceptance rate was 0.018, the number of particles was 982, and the effective sample size ESS=651.

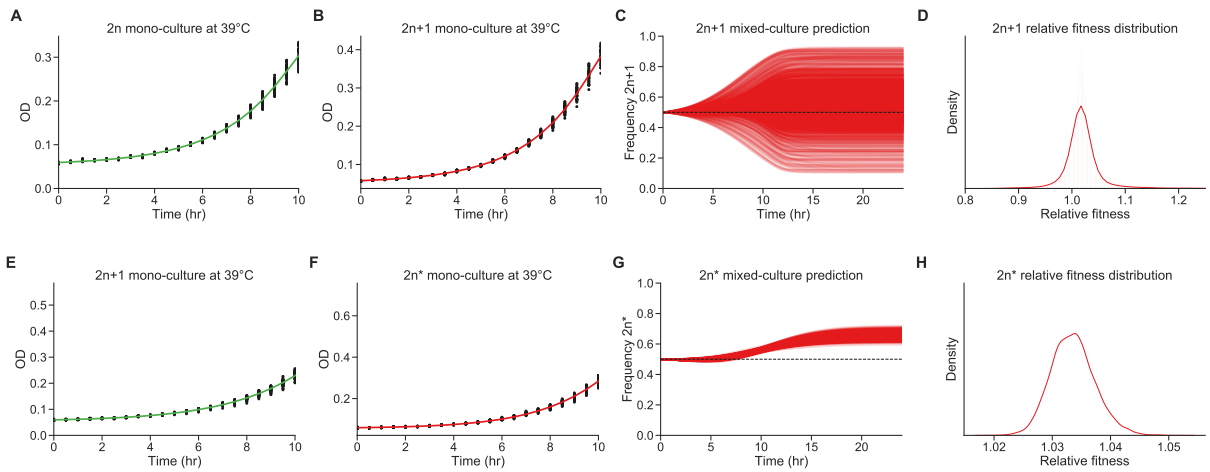


Figure S3: Fitness estimation from growth curves. **(A-D)** Fitness estimation from growth curves of $2n$ and $2n+1$ at 39°C . $w_{2n+1}/w_{2n}=1.024$ (95% CI: 0.959 - 1.115). **Curveball (E-H)** Fitness estimation from growth curves of $2n+1$ and $2n^*$ at 39°C . $w_{2n^*}/w_{2n+1}=1.033$ (95% CI: 1.027 - 1.041). Growth curves previously described in Yona et al.⁵¹, Figs. 3C, 4A, and S2. Fitness estimated from growth curves using Curveball, a method for predicting results of competition experiments from growth curve data²⁸ curveball.yoavram.com. See *Models and Methods, Prior distributions* for more details. **(A,B;E,F)** Mono-culture growth curve data (markers) and best-fit growth models (lines). **(C,G)** The mixed-culture prediction for the strains from A,B and E,F respectively, 6,375 generated curves. **(D,H)** The relative fitness distribution for $2n+1$ relative to $2n$ (panel D) and $2n^*$ relative to $2n+1$ (panel H). Figures generated by Curveball.

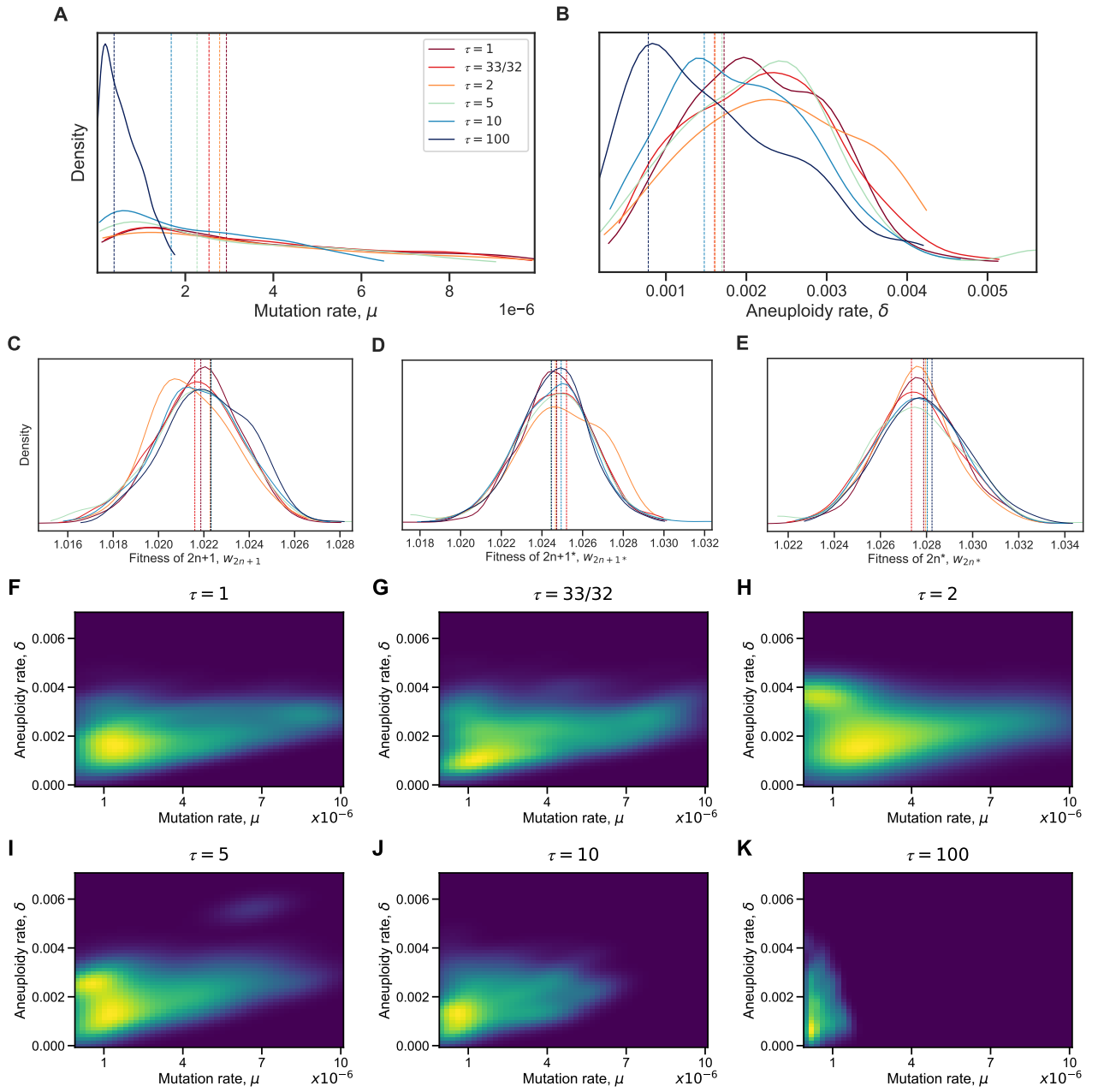


Figure S4: Model with elevated mutation rate in aneuploid cells. (A-E) The inferred posterior distributions for models with different values of τ , the fold-increase in mutation rate in aneuploid cells ($2n+1$ and $2n+1^*$). Vertical dashed lines represent the MAP (maximum a posteriori) of each distribution. When the increase in mutation rate is high, $\tau = 10$ and $\tau = 100$, the inferred mutation (A) and aneuploidy (B) rates tend to be lower. (F-K) The inferred joint posterior distribution of mutation rate (μ) and aneuploidy rate (δ) with different τ values (dark purple and bright yellow for low and high density, respectively).

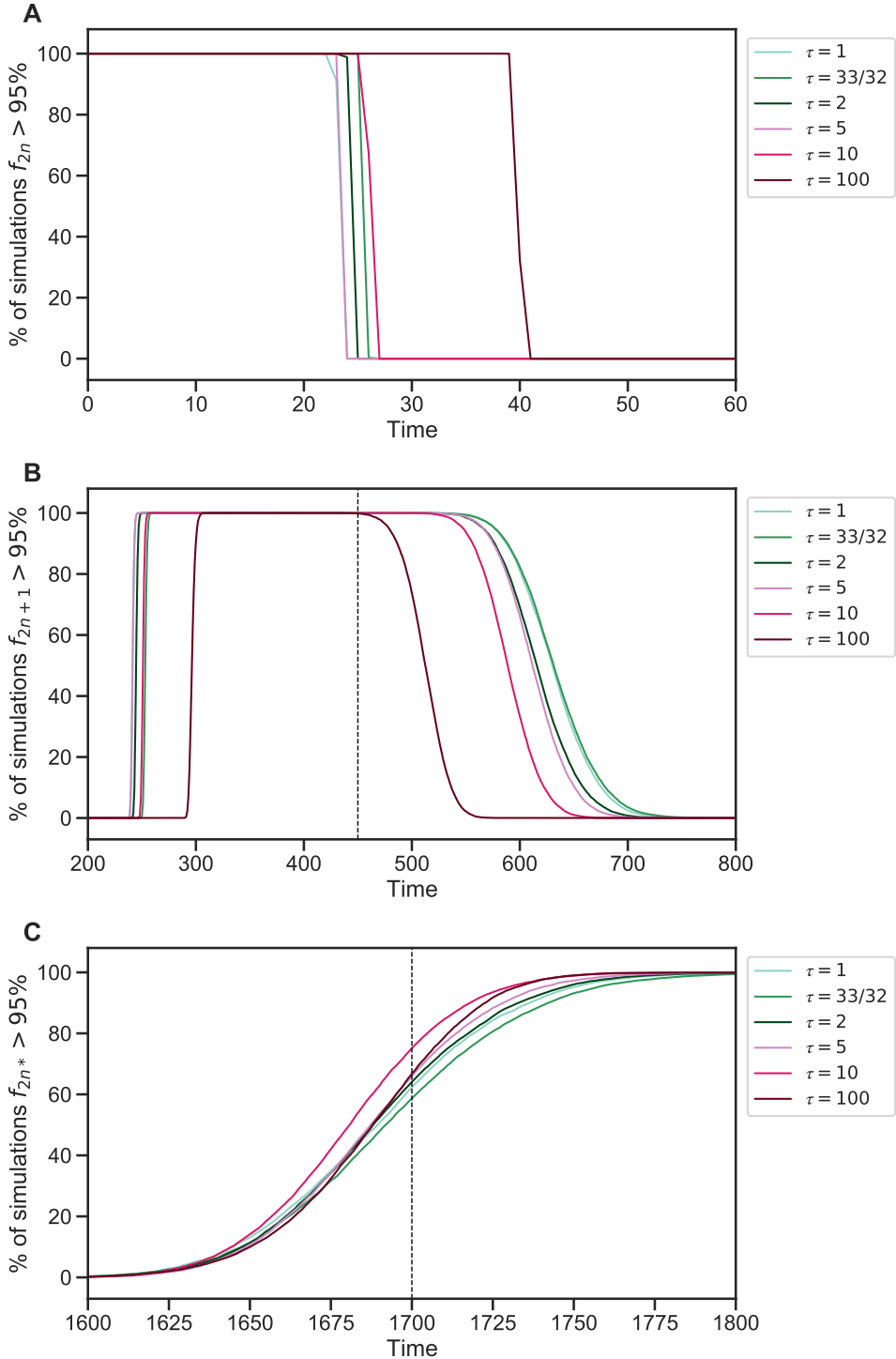


Figure S5: Genotype fixations for models with increased genetic instability. We estimated the parameters for different models, each assuming a different value of τ , the fold-increase in mutation rate in aneuploid cells. We then generated 10,000 simulations using the MAP estimate of each model and evaluated the fraction of simulations in which the frequency of genotype $2n$ (**A**), $2n+1$ (**B**), and $2n^*$ (**C**) is above 95% (y-axis) at each generation (x-axis). Note that $2n+1^*$ did not fix. We can see that $\tau = 100$ can be distinguished if the waiting time for $f_{2n} < 95\%$ is known (panel A) or if the waiting time for $f_{2n+1} > 95\%$ or $f_{2n+1} < 95\%$ is known (panel B). It is harder to distinguish between $1 \leq \tau \leq 10$.

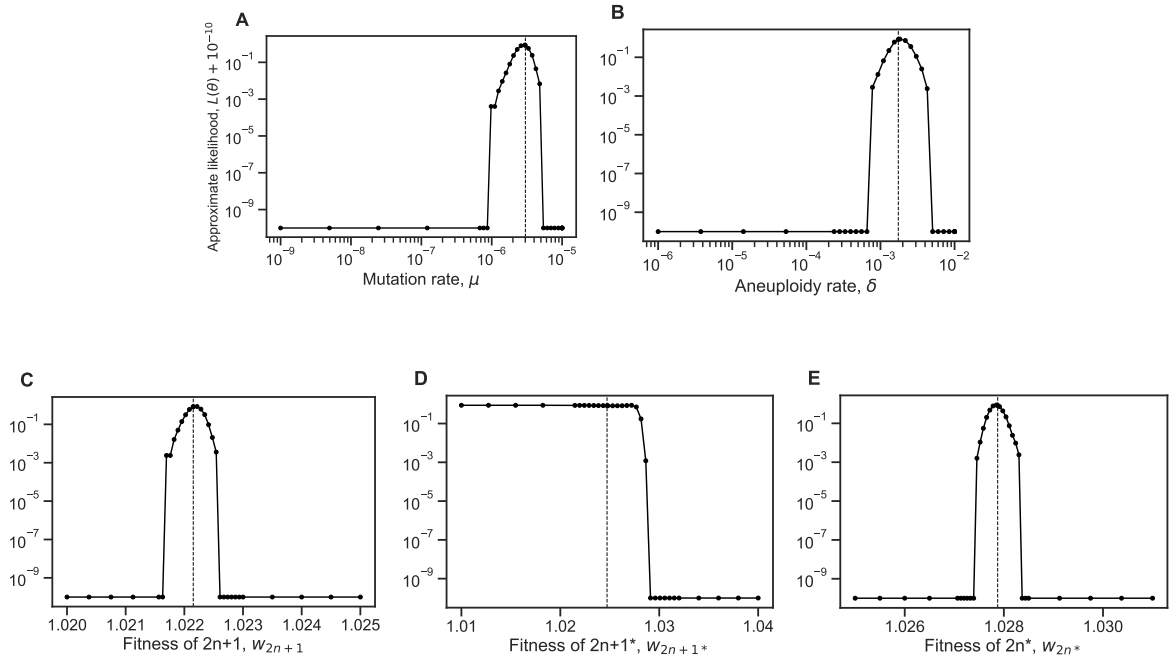


Figure S6: Likelihood profiles. Sensitivity of the model approximate likelihood, $\mathcal{L}(\theta)$, to changing a single parameter while the other parameters remain fixed at their MAP estimates. Dashed vertical line represents the MAP value. The prior distributions for the mutation rate and aneuploidy rate are $\mu \sim U(10^{-9}, 10^{-5})$ and $\delta \sim U(10^{-6}, 10^{-2})$, respectively.

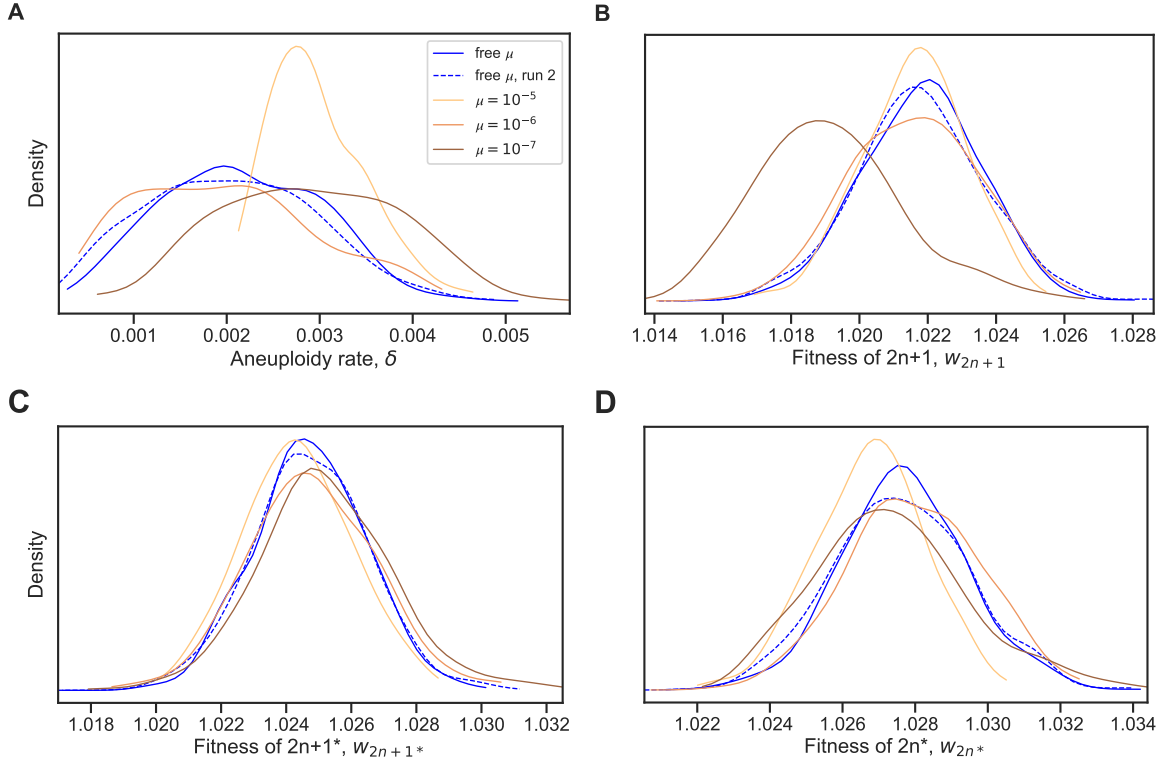


Figure S7: Model with fixed mutation rate. (A-D) The inferred posterior distributions for models with free and fixed mutation rate, μ . The MAP (maximum a posteriori) and 50% HDI (highest density interval) for each model are: **free μ , run 1:** $\delta = 2.749 \cdot 10^{-3}$ [$1.476 \cdot 10^{-3} - 2.822 \cdot 10^{-3}$], $w_{2n+1} = 1.022$ [1.021–1.023], $w_{2n+1}^* = 1.025$ [1.023–1.026], $w_{2n}^* = 1.027$ [1.026–1.029]; **free μ , run 2:** $\delta = 1.938 \cdot 10^{-3}$ [$1.338 \cdot 10^{-3} - 2.748 \cdot 10^{-3}$], $w_{2n+1} = 1.022$ [1.02–1.023], $w_{2n+1}^* = 1.025$ [1.023–1.026], $w_{2n}^* = 1.027$ [1.026–1.029]; **$\mu = 10^{-5}$:** $\delta = 3.089 \cdot 10^{-3}$ [$2.412 \cdot 10^{-3} - 3.169 \cdot 10^{-3}$], $w_{2n+1} = 1.022$ [1.021–1.023], $w_{2n+1}^* = 1.024$ [1.023–1.026], $w_{2n}^* = 1.027$ [1.026–1.028]; **$\mu = 10^{-6}$:** $\delta = 1.413 \cdot 10^{-3}$ [$1.04 \cdot 10^{-3} - 2.529 \cdot 10^{-3}$], $w_{2n+1} = 1.021$ [1.02–1.023], $w_{2n+1}^* = 1.024$ [1.023–1.026], $w_{2n}^* = 1.028$ [1.026–1.029]; **$\mu = 10^{-7}$:** $\delta = 3.4 \cdot 10^{-3}$ [$2.043 \cdot 10^{-3} - 3.578 \cdot 10^{-3}$], $w_{2n+1} = 1.019$ [1.017–1.02], $w_{2n+1}^* = 1.026$ [1.024–1.027], $w_{2n}^* = 1.027$ [1.026–1.029].

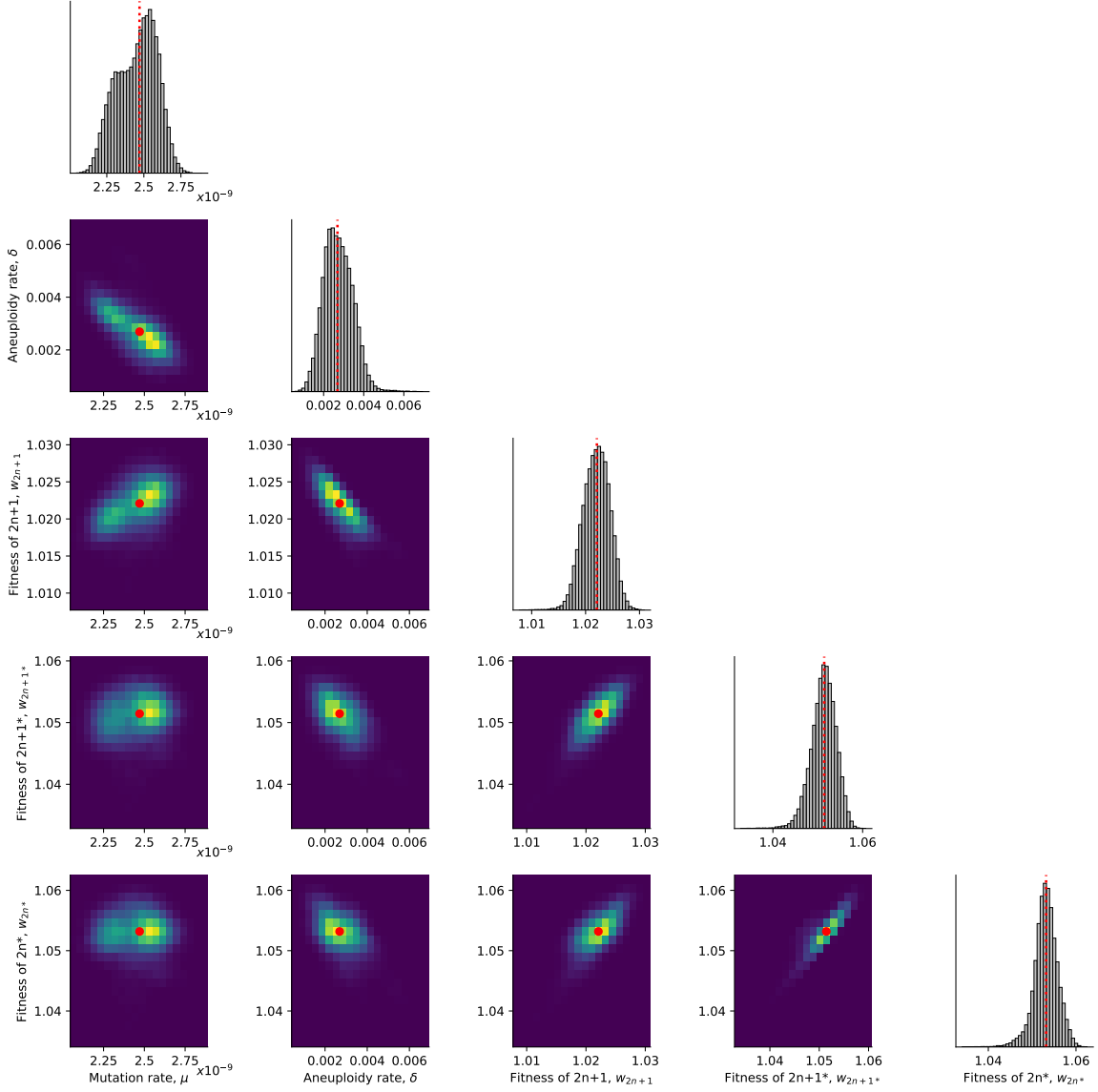


Figure S8: Posterior distribution of parameters inferred with the extended prior distribution. On the diagonal, the inferred posterior distribution of each model parameter. Below the diagonal, the inferred joint posterior distribution of pairs of model parameters (dark purple and bright yellow for low and high density, respectively). Red markers and orange lines for the joint MAP estimate (which may differ from the marginal MAP, as the marginal distribution integrates over all other parameters).

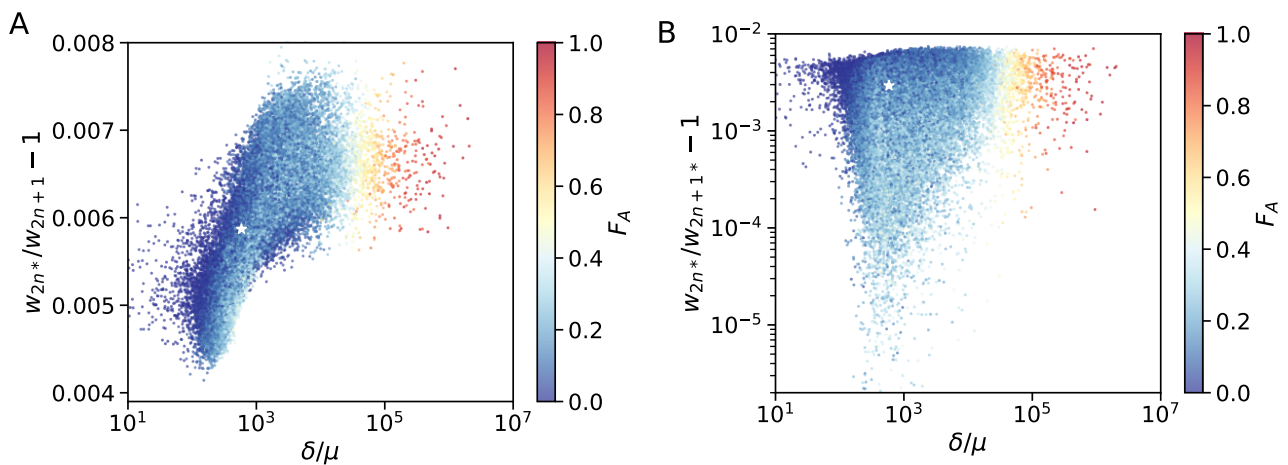


Figure S9: Posterior distribution of F_A . (A,B) F_A values (color coded) as in Figure 5 for different parameter choices on the x- and y-axes. White star denotes the MAP estimate.